A Design and Characterization Method of a Scalable Large Transmitting Array for Wireless Power Transfer

Young-Seok Lee, *Graduate Student Member, IEEE*, Taeyeong Yoon, *Graduate Student Member, IEEE*, Minje Kim, *Graduate Student Member, IEEE*, Sanghun Lee, *Graduate Student Member, IEEE*, Byungwook Jung, *Member, IEEE*, Jungsuek Oh, *Senior Member, IEEE*, and Sangwook Nam, *Life Senior Member, IEEE*

***Abstract*— This article presents a novel method for designing, characterizing, and calibrating a scalable transmitter with a large number of antenna elements, and for calculating the precise beam collection efficiency (BCE) in radio frequency wireless power transfer (WPT) systems. Rather than simply applying conventional calibration methods from radar systems to WPT systems, this article proposes an efficient calibration technique that reduces calibration time while accurately estimating BCE. The proposed method uses only a single connection at the transmitter array (TXA) input and a fixed reference antenna for WPT calibration, maintaining a simple experimental setup. This approach significantly reduces the time required for calibration and minimizes the space needed. Furthermore, to efficiently distribute RF signals in large array systems while minimizing space requirements, we present a loss compensated series power divider (LCSPD). Our approach is validated using an experimental prototype operating at 5.64 GHz, comprising a 256-element TXA and a 35-element receiver array (RXA). The calibration method's effectiveness is demonstrated through wireless power transmission experiments employing convex optimized (CVX) patterns at the transmitter. Comparative analysis of simulated and measured received power, using root-mean-squared error (RMSE) and normalized RMSE (NRMSE), shows a high correlation in RXA patterns. In a 0.5-m transmission scenario, we achieved a transmitted power of 6.08 W, received power of 4.37 W, and a BCE of 71.9%, underscoring the potential of near-field focusing in WPT systems and the accuracy of our proposed method.**

***Index Terms*— Array calibration, beam collection efficiency (BCE), large array, near-field focusing, wireless power transfer.**

I. Introduction

RADIO frequency wireless power transfer (RF-WPT, hereafter referred to as WPT), also known as microwave power transmission (MPT), is a technology that enables the delivery of energy over distances to a wide range of devices, from small sensors to large-scale electronics [1], [2], [3]. Several notable demonstrations have been made in this field: Hu et al. [4] developed a WPT system using the time-reversal method, capable of automatically tracking a slowly moving receiver. Operating at 2.45 GHz with a nine-element transmitter array (TXA), they transmitted 11.7 W of RF power and received 0.37 W at a single receiver 1 m away. Koo et al. [5] proposed a retroreflective TXA and its calibration method, achieving a received RF power of 0.45 W at distances up to 4 m, using a 64-element TXA operating at 5.2 GHz with 32-W total transmitted RF power. Belo et al. [6] demonstrated a far-field WPT system at 5.8 GHz based on lookup table selection, where the TXA radiated 1.3 W of RF power, resulting in 7 mW of received RF power at a 4-m distance.

A critical factor in determining the performance of WPT systems is the beam collection efficiency (BCE) [7], [8], [9]. BCE is also referred to as over-the-air (OTA) efficiency [4] or power transmission efficiency (PTE) [10], [11], and is a key metric in WPT systems [12]. It is defined as the ratio of the total power received at the receiver array (RXA) to the total power radiated by the TXA. This efficiency measure is essential for evaluating and optimizing the overall performance of WPT systems, providing a comprehensive assessment of the system's ability to transfer power wirelessly. The study of BCE has been approached through various theoretical methodologies, from pioneering work by Goubau and Schwering [13], [14] and Borgiotti [15] introducing the concept of efficiency demarcation at the apertures of the TXA and RXA within the Fresnel zone, to more practical studies focusing on planar array configurations, which have led to diverse methods for calculating efficiency, including the resolution of eigenvalue problems [7], [8], the application of chaotic particle

Received 13 August 2024; revised 10 October 2024; accepted 23 October 2024. This work was supported in part by the A-Laboratory, Samsung Electronics (50%) and in part by the Institute of Information and Communications Technology Planning and Evaluation (IITP) grant funded by the Korea Government (MSIT) through Advanced and Integrated Software Development for Electromagnetic Analysis (50%), under Grand 2019-0-00098. This article is an expanded version from the 2024 IEEE Wireless Power Transfer Technology Conference and Expo, Kyoto, Japan, 8–11, May, 2024 [DOI: 10.1109/WPTCE59894.2024.10557392]. *(Corresponding author: Sangwook Nam.)*

Young-Seok Lee, Taeyeong Yoon, Minje Kim, Sanghun Lee, Jungsuek Oh, and Sangwook Nam are with the Institute of New Media and Communication (INMC) and the Department of Electrical and Computer Engineering, Seoul National University, Seoul 08826, South Korea (e-mail: ryanlee@snu.ac.kr; taeyeong.yoon@snu.ac.kr; sbi06035@snu.ac.kr; sanghun8.lee@snu.ac.kr; jungsuek@snu.ac.kr; snam@snu.ac.kr).

Byungwook Jung is with Samsung Electronics, Suwon 16677, South Korea (e-mail: bw.jung@samsung.com).

Color versions of one or more figures in this article are available at https://doi.org/10.1109/TMTT.2024.3487911.

Digital Object Identifier 10.1109/TMTT.2024.3487911

swarm optimization [16], and the utilization of convex (CVX) optimization techniques [17], [18], significantly advancing our understanding of BCE in RF-WPT systems and providing valuable tools for system optimization.

The insights from these theoretical investigations have been integrated into WPT hardware systems, leading to practical demonstrations. For instance, Hu et al., in their previously mentioned study, reported a BCE of 3.2% for their system [4], benchmarking their performance against other relevant studies in the field [5], [6], [19], [20]. Hui et al. [21] achieved a higher efficiency of 60% for their system. Additional studies have further demonstrated WPT systems with notable achievements in both transmit and receive power [22], [23], [24], [25], [26], [27], showcasing the practical applications of theoretical advancements in WPT technology.

However, the method of calculating transmitted power in the aforementioned studies—by merely multiplying the estimated transmit power by the number of TXA elements—oversimplifies the reality, despite its importance in determining WPT system performance. Variations in impedance mismatches along the RF paths and antennas can lead to discrepancies in both the radiation magnitude and phase. Besides, these misalignments are likely to be exacerbated if magnitude tapering is employed, resulting in greater inaccuracies in the estimation of transmitted power. Furthermore, various researches commonly fix the magnitude in their maximum power, because of its hardware complexity. However, the magnitude tapering is essential for improving the BCE, which can achieve more received power while maintaining the transmitted power. Considering these limitations, more precise methods are required to estimate the total transmitted power, especially in scenarios with nonuniform transmit patterns. All transmitter antennas should ideally radiate with the same magnitude and phase, given a single common source. However, the TXA's complex composition, including RF distribution networks, parallel or series stages, and interconnections, leads to varying characteristics for each transmitter antenna after hardware integration. These disparities in RF signal lines from the source to individual antennas result in magnitude and phase offsets, necessitating compensation through transmitter calibration. While previous WPT works have just employed well-known array calibration techniques, such as rotating element electric field (REV) or multielement phase toggle (MEP) [28], [29], [30], [31], [32], [33], [34], this article proposes a simpler and more effective approach. Our method adopts an LUT that denotes power information, facilitating magnitude, and phase offset calibration. Unlike some conventional methods that require additional structures, our proposed calibration uses only a single connection at the TXA input and a fixed reference antenna. Furthermore, by comprehensively listing all radiated signals' magnitude and phase in the LUT, we can determine accurate transmitted power. This enables immediate calculation of BCE, even when the transmit pattern undergoes rapid changes due to continuous movement of the RXA in real-time systems. Our approach, thus, offers a more streamlined and adaptable solution for calibrating and optimizing WPT systems.

Additionally, we observed that existing WPT prototypes commonly employ parallel power dividers, such as Wilkinson power dividers, for RF signal distribution. While these parallel dividers are suitable for small arrays, their hardware complexity increases rapidly in larger arrays due to the bigger footprint necessitated by multiple connections. To address this issue, we propose a power divider with cascading structures, allowing for easy extension of signal distribution by simply connecting additional dividers in series. This approach reduces the width of the distribution line, making large transmitters more scalable. While Hu et al. [4] also proposed a cascading structure, their implementation was limited to a nine-element transmitter, constraining its potential for expansion. In contrast, we have demonstrated our power distribution method with a 256-element TXA, which can be considered a large array, thus showcasing the scalability and efficiency of our approach in handling more complex WPT systems.

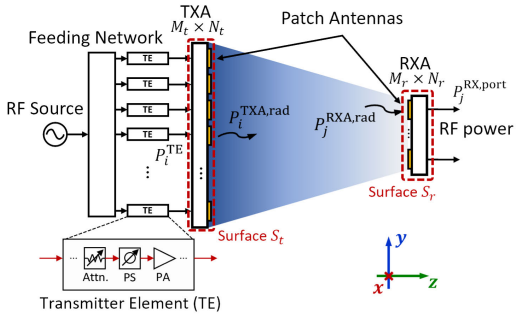

Fig. 1. Illustration of an overall conventional WPT system employing beamfocusing in the near-field region, where Attn., PS, and PA represent the attenuator, phase shifter, and power amplifier, respectively.

This article is an expanded version of our previous work [35]. Since our prior study mainly focused on the calibration methodologies, this expanded version provides a more detailed explanation of the proposed calibration and furthermore broadens our research scope by incorporating the following key components as contributions.

1) *Simple Calibration and Its Complexity Reduction [35] With Details:* Proposed an efficient calibration technique that uses only a single connection at TXA input and fixed reference antenna for WPT calibration, thus maintaining a simple experimental setup.
2) *Loss Compensated Series Power Divider (LCSPD):* Designed a loss compensated SPD to reduce the size of RF signal distribution and compensate transmission line loss for equal power distribution, making the transmitter array scalable.
3) *Accurate BCE Calculation:* Utilizes a calibration LUT validated for the precise calculation of BCE.
4) *System Implementation:* Confirms the validity of the proposed method by wireless power transfer experiments in near-field regions with CVX patterns.

II. System Overview

Consider a WPT system consisting of an $M_t \times N_t$ size TXA and an $M_r \times N_r$ size RXA, as illustrated in Fig. 1. The RF signal from the source is distributed by a feeding network,

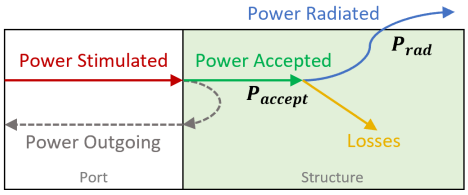

Fig. 2. Stimulated power flow in an antenna system.

with the magnitude and phase amplified and shifted by TEs.[1] The signal is then radiated from the antenna and received at the receiver. Building upon the theoretical studies presented in [13], [14], [15], [16], [17], and [18], we define the BCE in this context as the ratio of the total received RF power at the receiver antennas to the total radiated RF power from the transmitter antennas. This can be expressed as

$$\eta\ (\%) = \frac{P_r}{P_t} \times 100 \tag{1}$$

where η is the BCE in percent, P_t and P_r are the total transmitted and received RF power, respectively. For systems operating in the far-field region, it is well-established to calculate the radiated power by simulating or measuring the antenna array patterns. However, recent WPT systems, including this work, operate in the near-field region due to their larger array sizes, making it quite inaccurate to estimate the power using conventional beamforming methods. Assuming low coupling of the array antenna, P_t and P_r can be derived by summing up all radiated powers from each antenna individually, which can be expressed as

$$P_t = \sum_{i=1}^{M_t \cdot N_t} P_i^{\text{TXA, rad}} \tag{2}$$

$$P_r = \sum_{j=1}^{M_r \cdot N_r} P_j^{\text{RXA, rad}} \tag{3}$$

where $P_i^{\text{TXA, rad}}$ and $P_j^{\text{RXA, rad}}$ are the radiated powers for the ith TXA antenna and jth RXA antenna, respectively (see the notation in Fig. 1). Directly measuring all radiated powers remains challenging, especially for larger arrays. To address this, we can modify our approach by using the antenna radiation efficiency. Fig. 2 illustrates the primary power flow within the antenna system [36], where the antenna radiation efficiency (η_{rad}) is defined as

$$\eta_{\text{rad}} = \frac{P_{\text{rad}}}{P_{\text{stimulate}}} \tag{4}$$

where $P_{\text{stimulate}}$ and P_{rad} are the stimulated power at the antenna port and the radiated power, respectively. It is then reasonable to formulate the radiated power by combining (1)–(3), which can be expressed as

$$P_t = \sum_{i=1}^{M_t \cdot N_t} P_i^{\text{TXA, rad}} = \sum_{i=1}^{M_t \cdot N_t} P_i^{\text{TE}} \cdot \eta_i^{\text{TX}} \tag{5}$$

[1]Fig. 1 illustrates a one-to-one connection between TEs and antennas for simplicity. However, this is the most conventional configuration. In practice, various connection structures have been explored in different studies, such as subarray systems with fewer TEs than antennas.

$$P_r = \sum_{j=1}^{M_r \cdot N_r} P_j^{\text{RXA, rad}} = \sum_{j=1}^{M_r \cdot N_r} \frac{P_j^{\text{RX, port}}}{\eta_j^{\text{RX}}} \tag{6}$$

where η_i^{TX} and η_j^{RX} are the radiation efficiencies of the ith TXA and jth RXA antennas, respectively, and P_i^{TE} and $P_j^{\text{RX, port}}$ represent the port powers of TXA and RXA, respectively. Thus, by measuring the port powers (P_i^{TE}, $P_j^{\text{RX, Port}}$) and using the radiation efficiencies (η_i^{TXA}, $\eta_j^{\text{RX, rad}}$), we can derive accurate values for P_t and P_r for BCE calculation.[2]

III. Wireless Power Transmitter

In this section, we present the detailed design and integration of the TXA and RXA in the following subsections. The power divider and antenna were simulated using Ansys HFSS, while the schematic and layout of the TE PCB were designed using Cadence Allegro OrCAD.

A. System Design

Fig. 3 illustrates the full block diagram of the system, operating at a frequency of 5.64 GHz. The TXA and RXA have sizes of 16 × 16 and 7 × 5, respectively, with 0.6λ element spacing.[3] The TXA comprises 256 active channels, each of which can be controlled independently. The RF signal is distributed by LCSPDs, which are connected by series–parallel structures. A 1:16 LCSPD is first connected to the RF source, dividing the signal's magnitude equally and maintaining phase consistency across each layer. Each layer contains an identical LCSPD, where a PA amplifies the signal again to feed the TE, matching its input power conditions. Each TE consists of an attenuator, phase shifter, and PA. The RXA contains only antenna arrays, with a 7 × 5 array distributed across 35 SMA ports. The received signal for each port is measured individually by a spectrum analyzer, while the others are terminated in 50 Ohms. For clarity, we denote the structure from the RF source to the output for each layer as "stage 1," and the remaining parts as "stage 2," as shown in the dotted box in Fig. 3.[4]

The system operates with a desktop overall, using microcontroller unit (MCU) chips to control the magnitude and phase of each TE individually. We employed the serial peripheral interface (SPI) protocol for inter-MCU communication and interfaced with the desktop via a universal asynchronous receiver/transmitter (UART). The stage 1 master MCU is connected via SPI to the stage 2 layer MCU, which, in turn, connects to each TE MCU, also via SPI. This setup allows digital data to be sequentially driven from the desktop to all 256 TEs, passing through three MCUs each. All MCUs

[2]The radiation efficiency varies depending on the antenna's location in the array, making it complex to simulate all radiation efficiencies, especially for the TXA. We will address this consideration during the calibration process in Section IV.

[3]The TXA size was determined to accommodate short- to mid-range WPT applications, specifically targeting mobile phone use. In this scenario, the distance between the TXA and RXA was set to 30 × 100 cm, with a goal of achieving over 70% BCE at 50 cm. Considering this, the TXA size was set to 50 × 50 cm^2, while the RXA size was set to 20 × 10 cm^2, which corresponds to the size of a typical mobile phone.

[4]For a better understanding of the overall structure, please refer to the images in Section III-B.

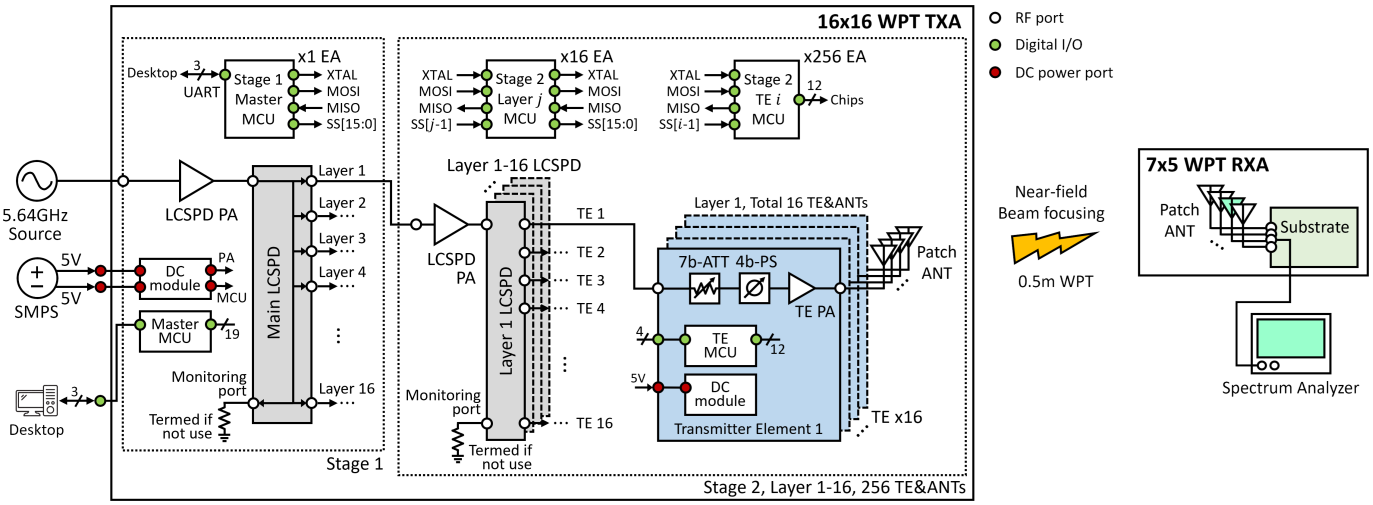

Fig. 3. Detailed block diagram of the proposed WPT system.

were programmed using Atmel Microchip Studio with C programming language, while MATLAB was used for full system control. Two SMPS units supply dc power, both providing 5 V to feed the PAs and MCUs, respectively.

The TE was designed to have a maximum output power (when no attenuation) of 32 dBm at the port, using a PCB substrate. We employed a low-cost 4-bit phase shifter with a 22.5° resolution, and a 7-bit attenuator with a maximum attenuation of 31.75 dB, allowing us to taper the magnitude with 0.25-dB linear steps.

The conventional design strategies for SPDs [37], [38] do not take into account the losses inherent in transmission lines. However, in practical applications, such as large-scale array systems, cumulative transmission line losses significantly degrade the ability of SPDs to distribute power equally. To address this issue, we propose an LCSPD topology, as illustrated in Fig. 4(a). To ensure equal phase distribution at each output port, the length of the transmission line connecting each output port is set to one guided wavelength. We first define the *power attenuation factor* $L = e^{-2\alpha l}$ for a transmission line of length l, where α can be extracted following [39]. Additionally, each port's power dividing ratio k_n (for $n = 1, \ldots, N$) related to the divided power P_n and the input power $P_{\text{in},n}$ is defined as $k_n = P_{\text{in},n}/P_n$. Therefore, the power at the port can be formulated as follows:

$$P_n = P\frac{L^{N-n}}{k_n - 1}\prod_{i=n}^{N}\left(1 - \frac{1}{k_i}\right)(n = 1, \ldots, N) \tag{7}$$

$$P_0 = PL^{N-1}L'\prod_{i=1}^{N}\left(1 - \frac{1}{k_i}\right) \tag{8}$$

where P_n and P_0 represent the power delivered to the output port and the monitoring port, respectively, while L' denotes the power attenuation factor at the monitoring port. For the equal power dividing condition at each output port with a 1:M unequal power dividing at the monitoring port, the power dividing ratio can be derived using the recurrence as follows:

$$P_N = P_{N-1} = \cdots = P_2 = P_1 = \frac{P_0}{M} \tag{9}$$

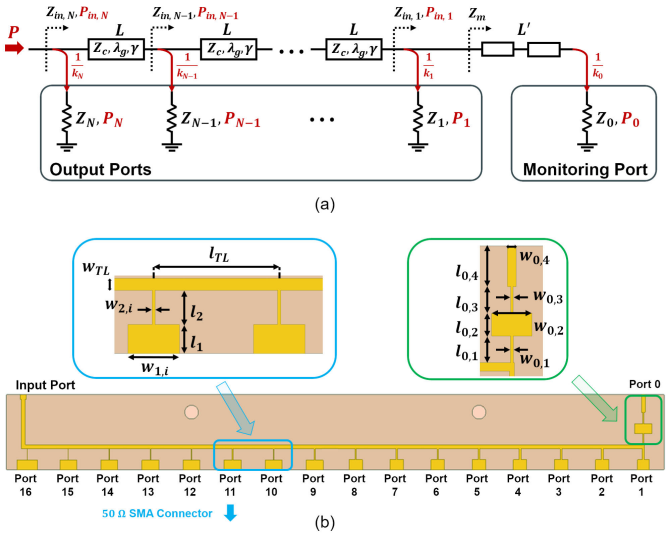

Fig. 4. (a) Equivalent circuit of LCSPD and (b) designed 1:16 LCSPD with monitoring port.

$$\begin{cases} (k_n - 1)L = k_{n-1} & \text{for } n = 2, \ldots, N \\ k_1 - 1 = \dfrac{M}{L'} & \text{for } n = 1. \end{cases} \tag{10}$$

$$k_n = L^{1-n}\left(\frac{M}{L'} + \frac{1}{1-L}\right) - \frac{L}{1-L}(n = 1, \ldots, N). \tag{11}$$

Following the power dividing ratio calculations, it is essential to consider the impedance characteristics to ensure the designed power distribution and impedance matching within the LCSPD. The input impedance at each node can be expressed as follows:

$$Z_{\text{in},n} = Z_n \parallel Z_c\frac{Z_{\text{in},n-1} + Z_c\tanh(\gamma l)}{Z_c + Z_{\text{in},n-1}\tanh(\gamma l)} \tag{12}$$

where $Z_{\text{in},n}$ is the input impedance at each node in the LCSPD, and Z_n represents the transmission line parameters and the load impedance at the preceding node. Since the transmission line length is set to be λ_g, (12) can be approximated as $Z_{\text{in},n} \approx Z_n \parallel Z_{\text{in},n-1}$. Therefore, load impedance at each output port

TABLE I
DESIGN PARAMETERS OF LCSPD

Parameters	Values (mm)
l_{TL}	28.15
w_{TL}	2.70
l_1	6.50
l_2	7.65
$w_{1,1}$	8.00
$w_{1,i}$ $(i = 2, \ldots, 8)$	9.20
$w_{1,i}$ $(i = 9, \ldots, 16)$	11.52
$w_{2,i}$ $(i = 1, \ldots, 16)$	1.4, 1.4, 1.3, 1.2, 1.1, 1.0, 0.9, 0.7, 0.825, 0.725, 0.625, 0.525, 0.425, 0.325, 0.225, 0.125
$l_{0,j}$ $(j = 1, 2, 3, 4)$	7.85, 6.64, 7.85, 11.96
$w_{0,j}$ $(j = 1, 2, 3, 4)$	0.80, 11.83, 0.70, 2.50

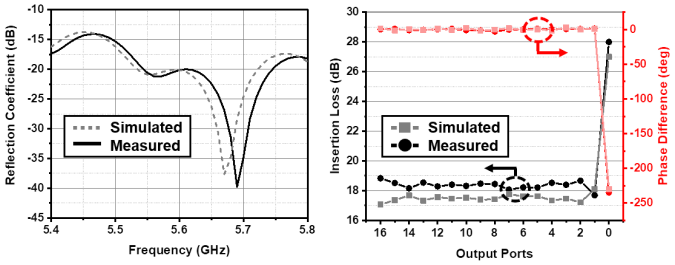

Fig. 5. Simulated and measured results of 1:16 LCSPD with monitoring port. (a) Reflection coefficient and (b) insertion loss (left axis) with phase difference (right axis) at operating frequency 5.64 GHz.

can be expressed as

$$Z_n = k_n Z_{\text{in},n} \approx k_n Z_n \parallel Z_{\text{in},n-1} = (k_n - 1)\frac{Z_{n-1}}{k_{n-1}} \tag{13}$$

$$Z_n = (k_n - 1)\left(\frac{k_{n-1} - 1}{k_{n-1}}\right) \cdots \left(\frac{k_1 - 1}{k_1}\right) Z_m. \tag{14}$$

From the recurrence relation about k_n with the input matching condition $Z_0 = Z_{\text{in},N}$, the load impedance Z_n at each output port and the required input impedance at the monitoring port Z_m can be determined by the transmission line loss and monitoring port power dividing ratio as follows:

$$\begin{cases} Z_n = Z_0 L^{N-n} k_N (n = 1, \ldots, N) \\ Z_m = Z_0 L^{N-1} k_N \dfrac{L'}{M}. \end{cases} \tag{15}$$

Fig. 4(b) shows the designed and fabricated 1:16 LCSPD with a monitoring port on FR-4 substrates ($\epsilon_r = 4.4$, $\tan\delta = 0.02$, $h = 1.6$ mm). The specific design parameters, presented in Table I, were determined through optimization to achieve the desired port impedance. The value of the extracted power attenuation factor is $L = 0.902$ (in linear). To achieve the calculated output port impedance Z_n and monitoring port impedance Z_m, we used two and four $\lambda/4$ transformers, respectively. Moreover, the losses of these transformers are not considered in our LCSPD formulations. The measurement results closely follow the simulation results, as shown in Fig. 5(a) and (b). In the measurement results, the input

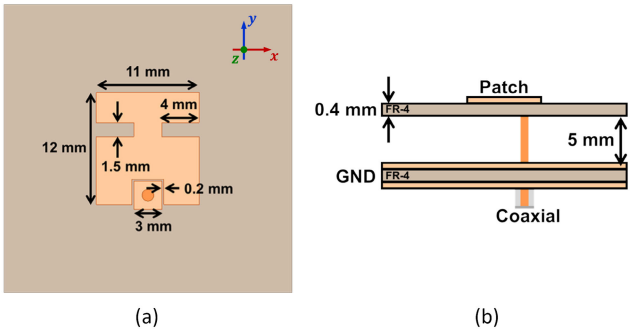

Fig. 6. (a) Top view and (b) side view of the proposed antenna.

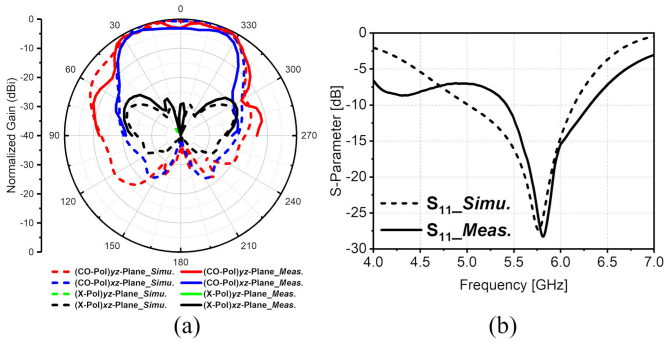

Fig. 7. Simulation and measurement results of (a) beam pattern and (b) *S*-parameter for the proposed antenna.

impedance is well-matched at 5.64 GHz. Among the output ports, we achieved an average insertion loss of 18.36 dB with a variation of 1.14 dB, while the phase variation is 4.33°. The theoretical insertion loss ($10\log P_n$) is calculated to be 15.92 dB. Notably, the insertion loss of the monitoring port is 28 dB, which allows us to monitor the distributed power at each layer without significant power degradation. These results demonstrate that the LCSPD design effectively distributes power while maintaining both magnitude and phase consistency and provides a monitoring capability with minimal impact on the main signal path. Furthermore, it is easy to expand the transmitter size by using only a single type of LCSPD, maintaining the small width of the RF distribution.

A single-element antenna, illustrated in Fig. 6, was designed using infinite boundary conditions realized by perfect electric conductor (PEC) and perfect magnetic conductor (PMC) boundaries to mimic the periodic characteristics of a large array. To achieve wide bandwidth, an air substrate-based capacitively indirect feeding structure was employed [40], [41], as shown in Fig. 6(a). Typically, coaxial cable-based feeding networks with a thick substrate have limited bandwidth due to the strong series inductance created by the inner conductor. To compensate for this, we implement indirect feeding (i.e., creating series capacitance); a combination of series and parallel resonance for the patch antenna can achieve bandwidth extension. Additionally, by using a slit on the aperture to reduce the size of the radiator, a coupling effect on the array can be achieved. This reduced aperture helps mitigate the coupling issue. Two thin FR-4 substrates ($\epsilon_r = 4.4$, $\tan\delta = 0.02$) were used to laminate copper [i.e., upper and lower

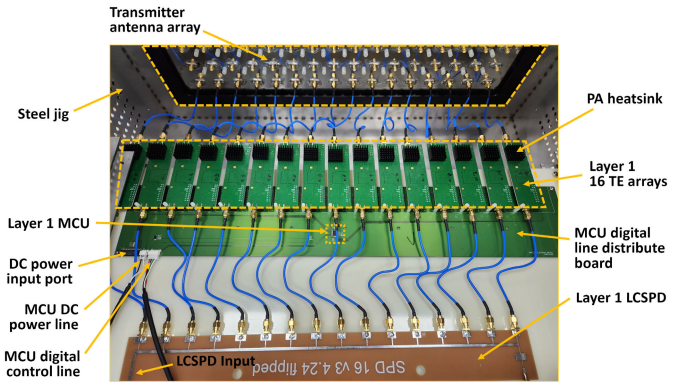

Fig. 8. Top-view of stage 2, layer 1 structure.

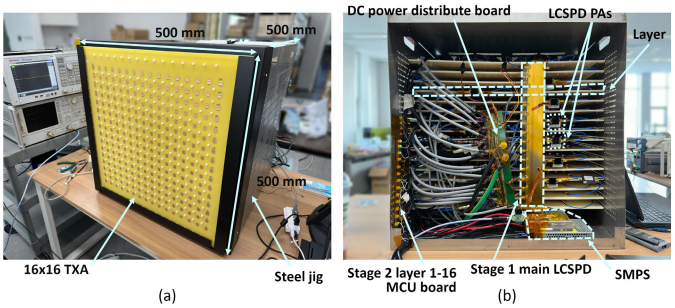

Fig. 9. Integrated 16 × 16 TXA. (a) Front view. (b) Rearview.

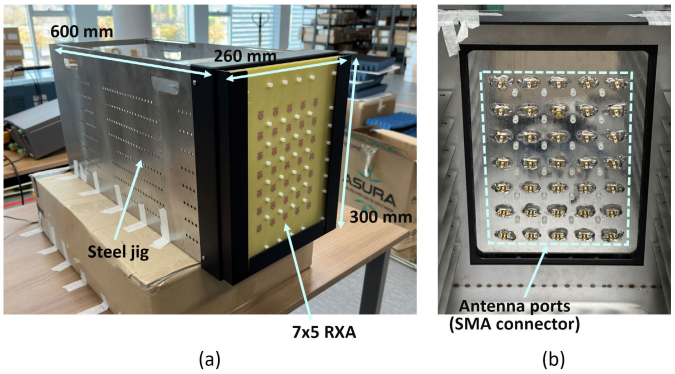

Fig. 10. 7 × 5 RXA. (a) Front view. (b) Rearview.

FR-4 for the patch and ground, respectively, as illustrated in Fig. 6(b)]; these FR-4 substrates were fixed using a nylon jig. Fig. 7(a) and (b) shows the beam pattern and impedance matching results of the proposed antenna, respectively. The half-power beamwidth (HPBW) is 70°, and the bandwidth extends from 4.9 to 5.9 GHz. The single element achieves a gain of 6 dBi and a radiation efficiency of 86%.

B. Hardware Integration

As shown in Fig. 8 and 9(b), 1 × 16 TEs horizontally constitute one layer, with 16 layers stacked vertically to construct the 16 × 16 TXA. Since the PA is a high-gain amplifier, each PA in the TE has a heatsink for rapid heat dissipation. Fig. 9(a) shows the front view of the TXA, which has dimensions of 500 × 500 × 500 mm^3. Fig. 9(b) displays the rear view of the TXA, where 16 layers are stacked vertically, and a single LCSPD is connected in parallel to feed all layers. It is worthwhile to note the proposed feeding network can be used repeatedly to extend TXA size (such as with 1024 elements) easily by cascading the network with TE modules. Two SMPS units are shown below, feeding the PAs and MCU, respectively. Additionally, since the 256 TE PAs consume massive energy, an additional dc power distribution board is vertically connected to feed power to each layer.

TABLE II
KEY COMPONENT PARAMETERS OF THE PROTOTYPE

Elements	Vendors	Type/Values
RF source	Analog Devices	EVAL-ADF4158
MCU	Microchip Technology	AVR32DB48
PA (SPD)	Skyworks Solutions	SE5004L_R
PA (TE)	Skyworks Solutions	SE5004L_EK1
Attenuator	Analog Devices	HMC1119LP4METR
Phase shifter	Macom	MAPS010145TR0500

The TXA was assembled in a steel jig, designed with space margins and numerous holes for heat dissipation. Fig. 10(a) and (b) shows the front and rear views of the RXA, respectively. The antenna shares the same shape as the TXA, except for its dimensions of 260 × 300 × 600 mm^3. Table II presents the parameters of the key components in the prototype.

IV. TRANSMITTER CALIBRATION

We previously developed a calibration method and a technique to reduce its complexity for WPT systems [35]. This method produces an LUT detailing the radiated power and phase from each antenna across all attenuation and phase shift conditions, effectively compensating for errors throughout the entire feeding network. In this section, we present the detailed calibration methodology and its validation process.

A. Calibration Methodology

The calibration process is outlined in Fig. 11(a). Two ports of a vector network analyzer (VNA) are connected to the transmitter's input and a single-receiver antenna, respectively, to measure the *S*-parameters for each configuration. During calibration, only one TE is activated at a time, with all others turned off, while the attenuator and phase shifter settings are automatically varied by MCU control. This process is repeated for all TEs.

Consider a single active antenna at TXA, marked as the ith antenna. As the signal travels through the system from the source, it experiences various types of path losses, such as power dividers, cables, and connectors. The components and the path that the signal travels through are marked in green and red in Fig. 11(a), respectively. Since all antennas share the same RF source, the difference in the radiating signal depends on the path (channel) from the input of TXA to the ith antenna. Our objective is to estimate the magnitude and phase characteristics at each transmitter antenna. The radiated magnitude and phase of each antenna can be derived by multiplying the RF input power by the channel. For the ith antenna, with attenuation and phase state (a, p)—which

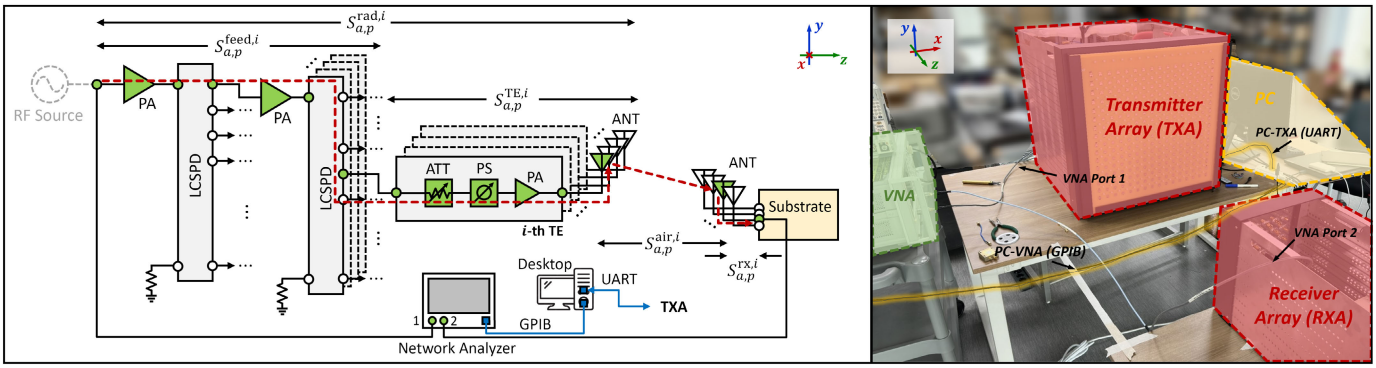

Fig. 11. (a) Block diagram of the proposed calibration setup. (b) Experimental setup.

represent the attenuation and phase states for the ith TE, respectively—the radiated signal can be expressed as

$$R_{a,p}^{\mathrm{rad},i} = S_{a,p}^{\mathrm{rad},i} \times S_{\mathrm{source}} \tag{16}$$

where $S_{a,p}^{\mathrm{rad},i}$ represents the channel from the RF source to the ith antenna of TXA for state (a, p), measured in units of volts per volt (V/V). $R_{a,p}^{\mathrm{rad},i}$ is the radiated signal from the ith antenna, measured in volts (V), and S_{source} is the magnitude of the RF source signal in volts (V). It is important to note that all these quantities are expressed in volts for unit consistency. Here, $S_{a,p}^{\mathrm{rad},i}$ can be calculated by dividing the channels from the air and the receiver side, which can be expressed as

$$S_{a,p}^{\mathrm{rad},i} = \frac{S_{a,p}^{\mathrm{VNA}}}{S_{a,p}^{\mathrm{rx},i} \cdot S_{a,p}^{\mathrm{air},i}} \tag{17}$$

where $S_{a,p}^{\mathrm{air},i}$ is the wave propagation channel (V/V), $S_{a,p}^{\mathrm{rx},i}$ is the channel from the receiver antenna to the port (V/V). Notably, $S_{a,p}^{\mathrm{VNA}}$ is the measured S_{21} from the VNA, and assuming the same impedance at each port, the unit is expressed as (V/V). The propagation channel $S_{a,p}^{\mathrm{air},i}$, assuming a free-space LOS scenario, can be derived from the Friis equation [42]. The magnitude (V/V) and phase (rad) are each formulated as

$$|S_{a,p}^{\mathrm{air},i}| = \sqrt{G_t(\theta_t, \phi_t) \cdot G_r(\theta_r, \phi_r)} \cdot \frac{\lambda}{4\pi R} \tag{18}$$

$$\angle S_{a,p}^{\mathrm{air},i} \equiv \mathrm{mod}(k \cdot R, 2\pi) \tag{19}$$

where G_t and G_r represent the linear scale antenna gains of the transmitter and receiver antennas, respectively, R is the distance between the two antennas in meter (m), and k is the wavenumber (rad/m). We can use this equation because the scenario involves two single antennas, which can be considered to be in the far-field region.

As mentioned in Section II, it is crucial to consider the radiated power from the transmitter antenna, not the port power. For large arrays, obtaining different radiation efficiencies for all transmitter antennas can be complicated. We can simplify this process by excluding the transmitter antenna gain from (18) as follows:

$$|S_{a,p}^{\mathrm{air},i}| = \sqrt{G_r(\theta_r, \phi_r)} \cdot \frac{\lambda}{4\pi R} \tag{20}$$

by excluding the transmitter antenna gain from the air channel $S_{a,p}^{\mathrm{air},i}$, then $S_{a,p}^{\mathrm{rad},i}$ can fully represent the radiated signal from the TXA, reversely. Since the definition of the BCE is based on the total radiated power from the TXA, it can accurately describe the radiated power. Consequently, the channel characterized at the receiver can be expressed as follows:

$$|S_{a,p}^{\mathrm{rx},i}| = \sqrt{\eta_{a,p}^{\mathrm{rx},i}} \tag{21}$$

where $\eta_{a,p}^{\mathrm{rx},i}$ is the receiver antenna's radiation efficiency. We use the square root because it is defined as a ratio of power. The phase is not considered in this equation because we can assume the same phase delay for all receiver antennas. This assumption is valid since the phase distribution of array antennas depends on relative phases, and the phase that passes through the receiver is relatively the same for all elements.

By aggregating the results from (16)–(21), we can measure and calculate the radiation magnitude and phase for all states (a, p). Using these data, we can construct an LUT that lists all the magnitude and phase information for each transmitter antenna. Algorithm 1 summarizes the complete process.

Once the LUT is created, the algorithm selects appropriate values based on the desired transmission pattern, including both magnitude and phase. Our approach prioritizes phase selection within a certain range first. From these phase candidates, we then select the combination with the closest magnitude match. This phase-prior selection method is implemented because there are various combinations in the LUT, and it allows us to more effectively navigate the finite resolution of the phase shifter and step attenuator.

B. Calibration Complexity Reduction

The process of building the LUT using the described procedures is effective but can be highly time consuming, especially for larger arrays. Since this method is designed for large array antennas, it is crucial to significantly reduce the calibration process. Thus, the main objective of this reduction is to streamline the creation of the LUT.

The fundamental approach to reducing complexity involves thoroughly measuring a single TE and extrapolating the results to the others. We designate the ith TE as the "Target TE" (TT, which is the TE at the green path described in Fig. 11). When

Algorithm 1 Generation of LUT

INITIALIZE: Turn OFF all TEs.
Command:
  Sel(*n*): Activate n-th TE, turn OFF all others.
  State(*a, p*): Set TE to state (a, p).
  Meas(*a, p*): Measure $S^{\text{VNA}}_{a,p}$ (from VNA to Desktop).
  V2P: Convert voltage to power scale (dBm, assuming 50 Ohm).
  Range: $1 \le n \le 256$, $1 \le a \le A$, $1 \le p \le P$.
Input:
  $C(n)$: Channel between n-th Tx ant. and Rx ref. ant.
  η: Rx antenna radiation efficiency.
  V: RF source signal (volts).
for $i = 1$ to 256 **do**
  Sel(i)
  for $j = 1$ to A **do**
    for $k = 1$ to P **do**
      State(j, k)
      LUT(i, j, k) $\leftarrow$ V2P(Meas(j, k) / [$C(i) \cdot \eta \cdot V$])
    end for
  end for
end for
Output: LUT(256, A, P)

set at a state (a, p), the total channel from the RF source to this point is $S^{\text{rad},i}_{a,p}$. This can be further expressed as

$$S^{\text{rad},i}_{a,p} = S^{\text{feed},i}_{a,p} \times S^{\text{TE},i}_{a,p} \tag{22}$$

where all three terms are in units of V/V. Due to the uniform manufacturing of TE boards, it is reasonable to assume consistent performance across all TEs. This assumption was further validated by the experimental demonstrations in our previous work in [35, Section III-A]. This allows us to simplify the notation as follows:

$$S^{\text{TE},i}_{a,p} \approx S^{\text{TE},j}_{a,p} (i \neq j) \tag{23}$$

furthermore, since $S^{\text{feed},i}_{a,p}$ remains constant across all states (a, p), we can simplify it as $S^{\text{feed},i}_{a,p} \approx S^{\text{feed},i}$. We select a single TE as the "Reference TE" (RT) and measure all $a \times p$ states for it. For any given state (a, p), the ratio of channels between the TT and RT can be simplified as follows:

$$\frac{S^{\text{rad},i}_{a,p}}{S^{\text{rad,ref}}_{a,p}} \approx \frac{S^{\text{feed},i}_{a,p}}{S^{\text{feed,ref}}_{a,p}} \approx S^{\text{feed}}_{i,\text{ref}} \tag{24}$$

where $S^{\text{feed}}_{i,ref}$ represents a fixed ratio that indicates the relationship between the two TEs. By applying this constant, we can derive all states for the TT from the comprehensive measurements of the RT. The extension of these states is formulated using (22)

$$S^{\text{rad},i}_{a^d,p^d} = S^{\text{rad,ref}}_{a^d,p^d} \times S^{\text{feed}}_{i,ref} \tag{25}$$

where (a^d, p^d) refers to the desired state for estimation. This method enables us to create a comprehensive LUT equivalent to measuring all states for all TEs, while actually performing full-state measurements on just one RT and single-state measurements on the other TEs. This approach significantly reduces the overall measurement time and complexity. Algorithm 2 summarizes the complete process.

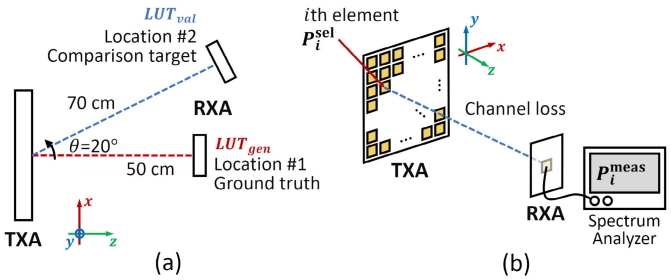

Fig. 12. LUT validation in two steps. (a) Replicating LUT build at various locations. (b) Cross-verifying power measurement.

Algorithm 2 Extension of LUT

INITIALIZE: Turn OFF all TEs.
Command: Shares with Algorithm 1.
Start reference TE scan:
  Choose $\forall s \in n$
  Sel(s);
  Repeat $\rightarrow$ for $j = 1 : A$; $k = 1 : P$;
    State(j, k);
    RT(j, k) $\leftarrow$ Meas(j, k) / [$C(i) \cdot \eta$];
  end
Start target TE scan:
for $i = 1$ to 256, except s **do**
  Sel(i);
  State(1,1);
  TT(j, k) $\leftarrow$ Meas(1,1) / [$C(i) \cdot \eta$];
end for
Use equation (25) for extension and build LUT.
Output: LUT(256, A, P)

C. Calibration Validation

The LUT was validated through a two-step process. First, to ensure stability regardless of the calibration location, we repeated the LUT generation at different locations. Fig. 12(a) illustrates this step, where the receiver is placed at different locations to simulate arbitrary scenarios. We repeated the LUT construction using the same procedures at two locations and conducted an analysis to assess the differences. The distances were set to 0.5 and 0.7 m, respectively, which are within the near-field region for the TXA and RXA, but sufficiently in the far-field for each individual antenna pair. These distances make it reasonable to use the Friis equation for channel estimation during the calibration process. The LUT built at location #1 was set as the ground truth (LUT_{gen}), and the LUT result at location #2 (LUT_{val}) served as the comparison target, from which we obtained the magnitude and phase differences. Second, we compared the LUT-based power with the measured power using a spectrum analyzer. Fig. 12(b) illustrates this setup, wherein the radiating power P^{sel}_i from the LUT allows us to estimate the received power P^{est}_i by performing a channel loss calculation as follows:

$$P^{\text{est}}_i = \frac{P^{\text{sel}}_i \times |S^{\text{air}}_i|^2}{\eta^{\text{rx}}} \tag{26}$$

where S^{air}_i represents the channel between two antennas, with the magnitude determined by (18), and η^{rx} is the radiation efficiency of the single-receiver antenna. It is important to note that all units are on the watt scale. By comparing the calculated

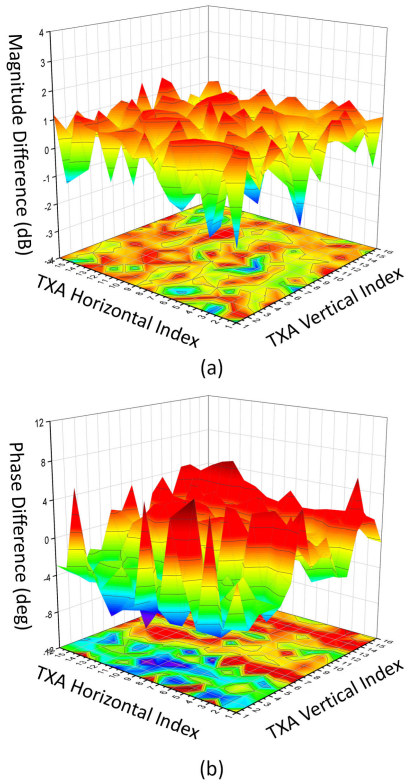

Fig. 13. LUT comparison by repeating the LUT building in different locations. (a) Magnitude difference (dB). (b) Phase difference (deg).

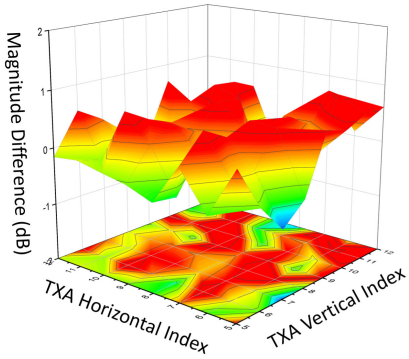

Fig. 14. Magnitude difference of the LUT-based simulation received power and measured power, units in dB.

P_i^{est} with the measured P_i^{meas}, we can validate the accuracy of the LUT's power predictions.

V. Experimental Results

In this section, we present the experimental results of the calibration validation, power transmission, and its calculated BCE with measurements. Additionally, we compare the BCE with other WPT research findings.

A. Measurement Validation

The calibration process generated an LUT detailing radiating powers and phases for 256 TEs across 21 attenuation levels (0–20 dB) and 16 phase settings (0–337.5°), using a VNA connected to a desktop via general purpose interface bus (GPIB). From the complexity reduction method, only 591 [21 × 16 + (256–1)] attempts were done during the 256-element transmitter calibration procedure. Initial validation was performed by comparing LUT_{gen} with LUT_{val}, where only attenuation of 0 dB and a phase state of "0" were shown for simplicity. Fig. 13 demonstrates that the magnitude variance lies within 2–3 dB, and the phase variance within "1" PS resolution (22.5°). Specifically, the average μ and standard deviation σ of the magnitude difference between LUT_{gen} and LUT_{val} were 0.49 and 0.88 dB, respectively.[5] These variations, which can occur due to VNA measurement errors, TXA and RXA alignment errors, or antenna pattern estimation errors, can be considered within acceptable margins.

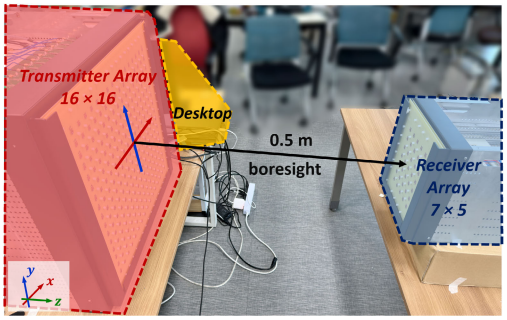

Fig. 15. Full-system configuration.

Fig. 14 presents the results of the second validation, where measurements using a spectrum analyzer were compared with LUT-based simulation results using MATLAB. TXA and RXA were positioned at location #1 [Fig. 12(a)]. The center 8 × 8 region of the TXA was selected,[6] and the received power measurement was taken at the center antenna of the RXA. The μ and σ of the difference were calculated as 0.22 and 0.45 dB, respectively. These results indicate that the LUT closely matches the measurements, thereby validating the LUT's accuracy.

B. Power Transmission

Fig. 15 illustrates the power transmission environment setup where the TXA and RXA are aligned in a line-of-sight (LOS) and boresight configuration at a distance of 0.5 m (where the RXA is in the near-field region of the TXA) for BCE calculation. The transmit pattern chosen was the CVX pattern, which optimizes the total received power by setting the total transmitted power as a constraint in a convex formulation [18]. This calculation was performed through MATLAB simulation, and an NVIDIA Tesla V100-32GB GPU was used to accelerate the CVX calculation, which was then implemented in the hardware system.

Fig. 16(a) displays the heatmap of the ideal CVX magnitude patterns in mW. The maximum element power of the pattern was normalized to 0.25 W [index (8, 8)]. After implementation in the hardware system, the nearest magnitude and phase

[5]Since the magnitude differences are derived in dB units, the μ and σ were calculated by transforming the scale into linear watt units, and then retransformed into dB.

[6]The first validation fully covered the TXA and included measurements at location #2, which corresponds to the outer portion. Therefore, measuring only the limited portion (the selected center 8 × 8 region) for the second validation is sufficient due to its measurement complexity.

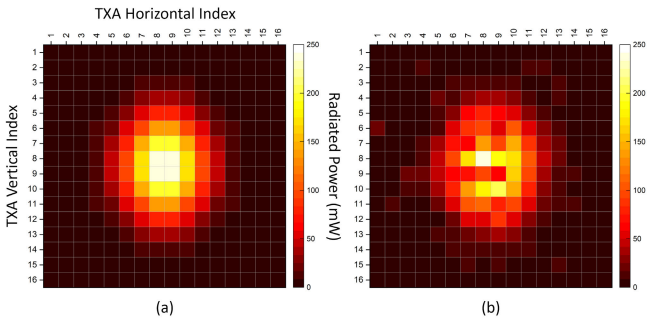

Fig. 16. Heatmap of TXA radiation power distribution using CVX pattern implementation, with units in mW. (a) Ideal pattern. (b) LUT-read pattern.

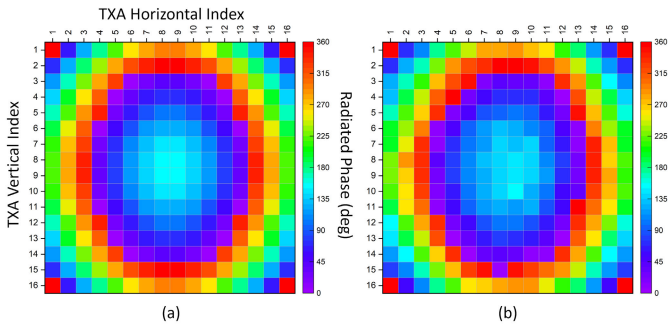

Fig. 17. Heatmap of TXA radiation phase distribution by CVX pattern implementation, with units in degrees. (a) Ideal pattern. (b) LUT-read pattern.

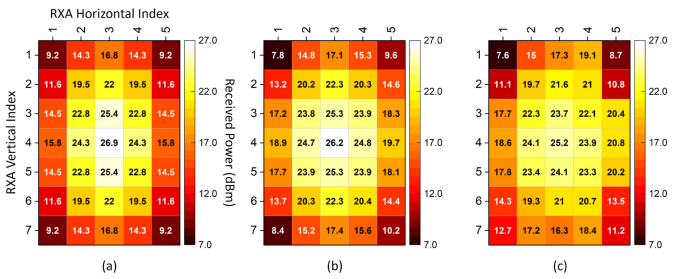

Fig. 18. Heatmap of RXA received power distribution, with units in dBm. (a) Ideal simulation. (b) Simulation pattern with LUT-read pattern. (c) Measured.

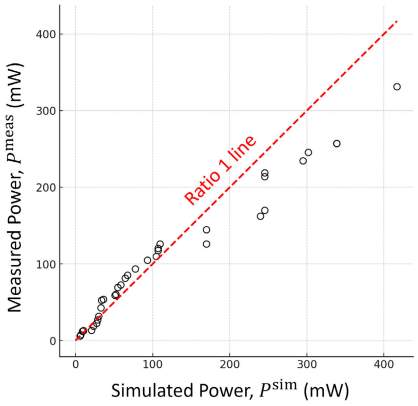

Fig. 19. Q–Q plot of the simulated and measured received patterns.

combination from the LUT was selected as the pattern.[7] Fig. 16(b) shows the result of the LUT-read CVX patterns, representing the power actually radiated by the TXA. The outliers in Fig. 16(b), which are antennas radiating less or more power than ideal, were caused by the unexpected cumulative mismatches in the RF path from the source, to major components, such as LCSPD, TE path, and until antenna. Fig. 17 presents the phase distribution for the CVX pattern, with both patterns aligned by the phase of element index (1, 1) at 360° (= 0°). The similarity between the patterns qualitatively demonstrates that the LUT values accurately describe the radiated pattern.

The CVX power pattern transmitted by the TXA was measured by a spectrum analyzer at the RXA, with all ports individually measured, while other ports were terminated. Fig. 18(a) shows the simulation result of the RXA received power pattern for the ideal CVX pattern, with units in dBm. Since the simulation assumes perfect TXA and RXA alignment and a nonreflective LOS environment, the result shows a clean symmetrical pattern. However, this pattern is not very meaningful due to its ideality. Fig. 18(b) displays the received RXA power pattern by simulation when the transmit pattern was used as the LUT-read data [Fig. 16(b) and 17(b)]. This simulation result is more comparable to the measured result shown in Fig. 18(c). Fig. 18(a)–(c) unified as port power since the measured result is obtained by port. The port power was derived by individually dividing the radiation efficiency of the RXA.

To validate the received power pattern, root-mean-squared error (RMSE) and its normalized form, NRMSE, were calculated between the simulation pattern of LUT-read and measured data quantitatively [Fig. 18(b) and (c)]. The equations are defined as follows:

$$\mathrm{RMSE} = \sqrt{\frac{1}{N}\sum_{i=1}^{N} |p_i^{\mathrm{sim}} - p_i^{\mathrm{meas}}|^2} \tag{27}$$

$$\mathrm{NRMSE} = \frac{\mathrm{RMSE}}{\max\left(P^{\mathrm{sim}}, P^{\mathrm{meas}}\right) - \min\left(P^{\mathrm{sim}}, P^{\mathrm{meas}}\right)} \tag{28}$$

where p_i^{sim} and p_i^{meas} are the simulated and measured power of RXA at each port, respectively, and P^{sim} and P^{meas} are the matrices of each pattern, respectively. N is the number of RXA elements, which is 35 in our case. The powers were converted into watt units to calculate the RMSE. NRMSE was considered to determine the effectiveness of the RMSE. The NRMSE defined in this article ranges from 0 to 1, where 0 indicates the same pattern and 1 indicates a completely different pattern. RMSE and NRMSE were calculated as 39.76 mW and 0.097, respectively. Additionally, the total power sum of the simulation result P_r^{sim} was 4.22 W and the measured P_r^{meas} was 3.76 W. Considering the RMSE, NRMSE, and the total received power, we can determine that the two patterns are closely distributed. Additionally, Fig. 19 represents the Q–Q plot, which qualitatively visualizes that the patterns are closely matched.

[7]As mentioned previously, the phase-prior algorithm was used for reading the LUT, which first finds the phase candidates within certain ranges and then selects the nearest magnitude. It cannot be said that this LUT-reading algorithm is the optimal one, but it is surely a simple and reasonable method.

TABLE III
COMPARISON OF RF-WPT SYSTEM PERFORMANCE

Ref.	RF power distribution	Frequency (GHz)	Algorithm	# of TXA elements	# of RX elements	TXA RF power (W)	RXA RF power (W)	BCE (%)	Distance (m)
[4]	Cascade	2.45	Time reversal	9	1	11.7	0.37	3.20	1.0
[5]	Parallel	5.2	Retroreflective	64	1	32	0.16	0.49	4.0
[6]	Parallel	5.8	Look-up Table	16	16	1.3	0.007	0.54	4.0
[19]	Parallel	2.4	Retrodirective	16	2	4	0.50	12.50	0.5
This work	Cascade	5.64	Look-up Table	256	35	6.08	4.37	71.86	0.5

The accurate BCE is then calculated using (5) and (6). The total TXA radiation power is derived by summing all the data in Fig. 16(b), resulting in a calculated P_t of 6.08 W. The total received RXA power is divided by the radiation efficiency of a single antenna. Given that the measured received power, P^{meas}, was 3.76 W, the BCE was calculated to be 71.9%. The simulated BCE, using the same transmitted power and P_r^{sim} for the received power, was calculated to be 80.7%.

The difference between the simulation and measured values is caused by various errors, realizing the high hardware complexity. Specifically, the dominant errors were due to misalignment between TXA and RXA during measurement, as the CVX pattern was generated in a simulation scenario with perfect alignment. Additionally, unavoidable reflections in the measurement environment, caused by the TXA being too large for anechoic chamber measurements, also contributed to the errors. However, the results show good similarity, as we tried to minimize the error at each step during measurement.

Table III provides a summary of our experiment compared with some selected previous works. Compared with these works, our approach shows the highest BCE and received power, utilizing our calibration methodology with the largest number of TXA elements. It is important to note that the RXA power in some previous works is described as port power, which makes the BCE less accurate.

VI. CONCLUSION

In this article, we address a method to design and characterize an expandable transmitter with a large number of antenna elements for WPT systems. An LCSPD was designed to distribute the RF signal effectively, reducing the size of a large array system and making the transmitter more easily scalable. Our approach incorporates a simple calibration and complexity reduction technique to generate an LUT that accurately predicts the radiated pattern, thereby enhancing system control efficiency. Addressing the limitations of existing methods for calculating BCE, we proposed a more accurate methodology for efficiency estimation based on calibration utilizing the LUT. We built a prototype operating at 5.64 GHz, with a TXA consisting of 256 elements and an RXA consisting of 35 elements. We validated the calibration method and demonstrated wireless power transmission using CVX patterns at the transmitter. Moreover, RMSE and NRMSE calculations for the RXA patterns were 39.76 mW and 0.097, respectively, showing high similarity between the simulation and measurements. The results showed a transmitted power of 6.08 W, a received power of 4.37 W, and a BCE of 71.9% in a scenario with a distance of 0.5 m. Our findings confirm that the proposed method closely aligns with ideal expectations and underscores the superiority of near-field focusing strategies.

REFERENCES

[1] W. C. Brown, "The history of power transmission by radio waves," *IEEE Trans. Microw. Theory Techn.*, vol. MTT-32, no. 9, pp. 1230–1242, Sep. 1984.
[2] W. C. Brown, "Experiments involving a microwave beam to power and position a helicopter," *IEEE Trans. Aerosp. Electron. Syst.*, vol. AES-5, no. 5, pp. 692–702, Sep. 1969.
[3] H. Matsumoto, "Research on solar power satellites and microwave power transmission in Japan," *IEEE Microw. Mag.*, vol. 3, no. 4, pp. 36–45, Dec. 2002.
[4] L. Hu et al., "Auto-tracking time reversal wireless power transfer system with a low-profile planar RF-channel cascaded transmitter," *IEEE Trans. Ind. Electron.*, vol. 70, no. 4, pp. 4245–4255, Apr. 2023.
[5] H. Koo et al., "Retroreflective transceiver array using a novel calibration method based on optimum phase searching," *IEEE Trans. Ind. Electron.*, vol. 68, no. 3, pp. 2510–2520, Mar. 2021.
[6] D. Belo, D. C. Ribeiro, P. Pinho, and N. B. Carvalho, "A selective, tracking, and power adaptive far-field wireless power transfer system," *IEEE Trans. Microw. Theory Techn.*, vol. 67, no. 9, pp. 3856–3866, Sep. 2019.
[7] N. Shinohara, "Beam efficiency of wireless power transmission via radio waves from short range to long range," *J. Electromagn. Eng. Sci.*, vol. 10, no. 4, pp. 224–230, Dec. 2010.
[8] S. Kojima, T. Mitani, and N. Shinohara, "Array optimization for maximum beam collection efficiency to an arbitrary receiving plane in the near field," *IEEE Open J. Antennas Propag.*, vol. 2, pp. 95–103, 2021.
[9] G. Oliveri, L. Poli, and A. Massa, "Maximum efficiency beam synthesis of radiating planar arrays for wireless power transmission," *IEEE Trans. Antennas Propag.*, vol. 61, no. 5, pp. 2490–2499, May 2013.
[10] J.-H. Kim, Y. Lim, and S. Nam, "Efficiency bound of radiative wireless power transmission using practical antennas," *IEEE Trans. Antennas Propag.*, vol. 67, no. 8, pp. 5750–5755, Aug. 2019.
[11] Y.-C. Kim, B.-H. Choi, and J.-H. Lee, "Comparative study on the power transfer efficiency of magnetic resonance and radio frequency wireless power transmission," *J. Electromagn. Eng. Sci.*, vol. 16, no. 4, pp. 232–234, Oct. 2016.
[12] B. Jiang, P. Li, S. Zheng, Y. Lin, and H. Xu, "A 24-GHz beam-steerable multinode wireless power transfer system with a maximum DC output of 5.7 dBm at 1-m distance," *IEEE Trans. Microw. Theory Techn.*, early access, May 27, 2024, doi: 10.1109/TMTT.2024.3402067.
[13] G. Goubau and F. Schwering, "On the guided propagation of electromagnetic wave beams," *IRE Trans. Antennas Propag.*, vol. 9, no. 3, pp. 248–256, May 1961.
[14] G. Goubau, "Microwawe power transmission from an orbiting solar power station," *J. Microw. Power*, vol. 5, no. 4, pp. 224–231, Jan. 1970.
[15] G. V. Borgiotti, "Maximum power transfer between two planar apertures in the Fresnel zone," *IEEE Trans. Antennas Propag.*, vol. AP-14, no. 2, pp. 158–163, Mar. 1966.

[16] X. Li, B. Duan, J. Zhou, L. Song, and Y. Zhang, "Planar array synthesis for optimal microwave power transmission with multiple constraints," *IEEE Antennas Wireless Propag. Lett.*, vol. 16, pp. 70–73, 2017.
[17] A. F. Morabito, A. R. Lagana, and T. Isernia, "Optimizing power transmission in given target areas in the presence of protection requirements," *IEEE Antennas Wireless Propag. Lett.*, vol. 14, pp. 44–47, 2015.
[18] H. Y. Kim, Y. Lee, and S. Nam, "Efficiency bound estimation for a practical microwave and mmWave wireless power transfer system design," *J. Electromagn. Eng. Sci.*, vol. 23, no. 1, pp. 69–74, Jan. 2023.
[19] P. D. H. Re, S. K. Podilchak, S. A. Rotenberg, G. Goussetis, and J. Lee, "Circularly polarized retrodirective antenna array for wireless power transmission," *IEEE Trans. Antennas Propag.*, vol. 68, no. 4, pp. 2743–2752, Apr. 2020.
[20] K. W. Choi et al., "Toward realization of long-range wireless-powered sensor networks," *IEEE Wireless Commun.*, vol. 26, no. 4, pp. 184–192, Aug. 2019.
[21] Q. Hui, K. Jin, and X. Zhu, "Directional radiation technique for maximum receiving power in microwave power transmission system," *IEEE Trans. Ind. Electron.*, vol. 67, no. 8, pp. 6376–6386, Aug. 2020.
[22] X. Wang, S. Sha, J. He, L. Guo, and M. Lu, "Wireless power delivery to low-power mobile devices based on retro-reflective beamforming," *IEEE Antennas Wireless Propag. Lett.*, vol. 13, pp. 919–922, 2014.
[23] J. He, X. Wang, L. Guo, S. Shen, and M. Lu, "A distributed retro-reflective beamformer for wireless power transmission," *Microw. Opt. Technol. Lett.*, vol. 57, no. 8, pp. 1873–1876, Aug. 2015.
[24] S. T. Khang, D. J. Lee, I. J. Hwang, T. D. Yeo, and J. W. Yu, "Microwave power transfer with optimal number of rectenna arrays for midrange applications," *IEEE Antennas Wireless Propag. Lett.*, vol. 17, no. 1, pp. 155–159, Jan. 2018.
[25] J. Bae et al., "LUT-based focal beamforming system using 2-D adaptive sequential searching algorithm for microwave power transfer," *IEEE Access*, vol. 8, pp. 196024–196033, 2020.
[26] X. Yi, X. Chen, L. Zhou, S. Hao, B. Zhang, and X. Duan, "A microwave power transmission experiment based on the near-field focused transmitter," *IEEE Antennas Wireless Propag. Lett.*, vol. 18, no. 6, pp. 1105–1108, Jun. 2019.
[27] C. Im, E. Kang, and H. Choo, "High-gain patch antenna with stacked director patches using an end-fire theory for microwave power transfer applications," *J. Electromagn. Eng. Sci.*, vol. 24, no. 4, pp. 411–417, Jul. 2024.
[28] G. Magalhes et al., "A novel calibration method for phased-array radar based on element-wise time offsetting and multi-element phase toggle," in *Proc. IEEE RadarConf.*, Boston, MA, USA, 2019, pp. 1–6.
[29] S. Mano and T. Katagi, "A method for measuring amplitude and phase of each radiating element of a phased array antenna," *Electron. Commun. Jpn.*, vol. 65, no. 5, p. 58, 1982.
[30] I. Chiba et al., "Phased array antenna calibration method in operating condition REV method," Jpn. Resour. Observ. Syst. Org., Mitsubishi Electr. Corp., Kanagawa, Japan, Tech. Rep., 1999, vol. 1, no. 85.
[31] T. Takahashi et al., "Fast measurement technique for phased array calibration," *IEEE Trans. Antennas Propag.*, vol. 56, pp. 1888–1899, Jul. 2008.
[32] T. Takahashi, Y. Konishi, and I. Chiba, "A novel amplitude-only measurement method to determine element fields in phased arrays," *IEEE Trans. Antennas Propag.*, vol. 60, pp. 3222–3230, Jul. 2012.
[33] G. Hampson and A. Smolders, "A fast and accurate scheme for calibration of active phased-array antennas," in *Proc. IEEE Antennas Propag. Soc. Int. Symp.*, vol. 2, Apr. 1999, pp. 1040–1043.
[34] I. Coşkun and S. Ikizoğlu, "Implementation possibilities of standard site method sub-cases for EMC antenna calibrations in non-ideal site conditions," *J. Electromagn. Eng. Sci.*, vol. 23, no. 4, pp. 369–377, Jul. 2023.
[35] Y.-S. Lee et al., "LUT-based transmit mode calibration complexity reduction method for wireless power transfer," in *Proc. IEEE Wireless Power Technol. Conf. Expo (WPTCE)*, Kyoto, Japan, May 2024, pp. 137–141.
[36] Dassault Systmes. (2021). *CST Studio Suite*. [Online]. Available: https://space.mit.edu/RADIO/CST_online/cst_studio_suite_help.htm
[37] E. A. Soliman, A. Vasylchenko, V. Volski, G. A. E. Vandenbosch, and W. D. Raedt, "Series-fed microstrip antenna arrays operating at 26 GHz," in *Proc. IEEE Antennas Propag. Soc. Int. Symp.*, Jul. 2010, pp. 1–4.
[38] D. Inserra, W. Hu, and G. Wen, "Design of a microstrip series power divider for sequentially rotated nonuniform antenna array," *Int. J. Antennas Propag.*, vol. 2017, p. 8, 2017, Art. no. 9482979, doi: 10.1155/2017/9482979.
[39] J. Zhang and T. Y. Hsiang, "Extraction of subterahertz transmission-line parameters of coplanar waveguides," *PIERS Online*, vol. 3, no. 7, pp. 1102–1106, 2007.
[40] T. Yoon and J. Oh, "Metal rod-based field concentrated common and differential modes theory enabling design of dual-polarized antennas," *IEEE Trans. Antennas Propag.*, vol. 71, no. 10, pp. 7782–7791, Oct. 2023.
[41] T. Yoon, U. Park, and J. Oh, "Band-stop behavior vertically extended ground isolator based on transmission line theory for IBFD TRx decoupling applications," *IEEE Trans. Microw. Theory Techn.*, vol. 72, no. 2, pp. 1405–1415, Feb. 2024.
[42] H. T. Friis, "A note on a simple transmission formula," *Proc. IRE*, vol. 34, no. 5, pp. 254–256, May 1946.

Young-Seok Lee (Graduate Student Member, IEEE) received the B.S. degree from the School of Electrical Engineering, Korea University, Seoul, South Korea, in 2021, and the M.S. degree from the Department of Electrical and Computer Engineering, Seoul National University, Seoul, in 2023, where he is currently pursuing the Ph.D. degree.

His current research interests include wireless power transfer systems, optimization algorithms, target detection, and indoor localization.

Taeyeong Yoon (Graduate Student Member, IEEE) received the B.S. degree (summa cum laude) in electronic engineering from Korea Aerospace University, Goyang, South Korea, in 2021, and the M.S. degree from the Department of Electrical and Computer Engineering, Seoul National University, Seoul, South Korea, in 2023, where he is currently pursuing the Ph.D. degree.

His current research interests include suppressing dual-polarized multipath coupling, dual-polarized antennas for sub-6-GHz applications, high-efficiency power amplifiers for millimeter-wave (mm-wave) applications, and RF/mm-wave/microwave integrated circuits.

Minje Kim (Graduate Student Member, IEEE) received the B.S. degree from the Department of Electrical and Computer Engineering, Seoul National University, Seoul, South Korea, in 2023, where he is currently pursuing the integrated master's and Ph.D. degree.

His current research interests include the generative AI for antenna inverse design and EMI/EMC prediction utilizing text-to-image diffusion model, series power divider modeling, and large-array wireless power transfer system.

Sanghun Lee (Graduate Student Member, IEEE) received the B.S. degree in electronic engineering from Kyungpook National University, Daegu, South Korea, in 2014. He is currently pursuing the M.S. degree at the Department of Electrical and Computer Engineering, Seoul National University, Seoul, South Korea.

Since 2014, he has been an RF Circuit Designer with Samsung Electronics, Suwon, South Korea. His current research interests include microwave power transmission and RF systems.

Byungwook Jung (Member, IEEE) received the Ph.D. degree from the Korea Advanced Institute of Science and Technology, Daejeon, South Korea, in 2010.

From 2010 to 2016, he was a Staff Engineer with LG Electronics, Seoul, South Korea. He joined Samsung Electronics, Suwon, South Korea, in 2017, where he is currently a Principal Engineer. His research interests include image generation, signal processing algorithms, and global optimization.

Jungsuek Oh (Senior Member, IEEE) received the B.S. and M.S. degrees from Seoul National University, Seoul, South Korea, in 2002 and 2007, respectively, and the Ph.D. degree from the University of Michigan at Ann Arbor, MI, USA, in 2012.

From 2007 to 2008, he was with Korea Telecom, Seongnam, South Korea, as a Hardware Research Engineer, where he was involved in the development of flexible RF devices. From 2013 to 2014, he was a Staff RF Engineer with Samsung Research America, Dallas, TX, USA, where he was a Project Leader for the 5G/millimeter-wave antenna system. He is currently an Associate Professor with the School of Electrical and Computer Engineering, Seoul National University, Seoul, South Korea. He has authored or co-authored more than 60 technical journal and conference articles. His research interests include mmWave beam focusing/shaping techniques, antenna miniaturization for integrated systems, and radio propagation modeling for indoor scenarios.

Prof. Oh was a recipient of the 2011–2012 Rackham Predoctoral Fellowship Award, the 2014 Samsung DMC R&D Innovation Award, the 2018 SNU Creative Researcher Award, the 2019 Samsung Electro-Mechanics Silver Prize, and the best paper awards from several conferences. He served as a TPC Member and the Session Chair for the IEEE AP-S/USNC-URSI and ISAP.

Sangwook Nam (Life Senior Member, IEEE) received the B.S. degree in electrical engineering from Seoul National University, Seoul, South Korea, in 1981, the M.S. degree in electrical engineering from the Korea Advanced Institute of Science and Technology, Seoul, in 1983, and the Ph.D. degree in electrical engineering from the University of Texas at Austin, Austin, TX, USA, in 1989.

From 1983 to 1986, he was a Researcher with the Gold Star Central Research Laboratory, Seoul. Since 1990, he has been a Professor with the School of Electrical Engineering and Computer Science, Seoul National University. His research interests include the analysis and design of electromagnetic structures, antennas, microwave active/passive circuits, and radar systems.